

Advanced Algorithms and High-Performance Testbed for Large-Scale Site Characterization and Subsurface Target Detection using Airborne Ground Penetrating SAR

Amir Fijany, James B. Collier, and Ari Citak
Jet Propulsion Laboratory, California Institute of Technology
MS 126-347, 4800 Oak Grove Drive
Pasadena, CA 91109
818-393-5342
Amir.Fijany@jpl.nasa.gov

Abstract - A team of US Army Corps of Engineers, Omaha District and Engineering and Support Center, Huntsville, Jet Propulsion Laboratory (JPL), Stanford Research Institute (SRI), and Montgomery Watson is currently in the process of planning and conducting the largest ever survey at the Former Buckley Field (60,000 acres), in Colorado, by using SRI airborne, ground penetrating, Synthetic Aperture Radar (SAR). The purpose of this survey is the detection of surface and subsurface Unexploded Ordnance (UXO) and in a broader sense the site characterization for identification of contaminated as well as clear areas. In preparation for such a large-scale survey, JPL has been developing advanced algorithms and a high-performance testbed for processing of massive amount of expected SAR data from this site. Two key requirements of this project are the accuracy (in terms of UXO detection) and speed of SAR data processing. The first key feature of this testbed is a large degree of automation and a minimum degree of the need for human perception in the processing to achieve an acceptable processing rate of several hundred acres per day. For accurate UXO detection, novel algorithms have been developed and implemented. These algorithms analyze dual polarized (HH and VV) SAR data. They are based on the correlation of HH and VV SAR data and involve a rather large set of parameters for accurate detection of UXO. For each specific site, this set of parameters can be optimized by using ground truth data (i.e., known surface and subsurface UXOs). In this paper, we discuss these algorithms and their successful application for detection of surface and subsurface anti-tank mines by using a data set from Yuma proving Ground, AZ, acquired by SRI SAR.

TABLE OF CONTENTS

1. INTRODUCTION
2. YUMA SAR DATA SET
3. JPL AUTOMATIC TARGET DETECTION ALGORITHM
4. RESULTS OF MINE DETECTION USING YUMA SAR DATA SET
5. CONCLUSION AND DISCUSSION OF FUTURE WORKS
6. ACKNOWLEDGEMENT
7. REFERENCES
8. BIOGRAPHY

1. INTRODUCTION

Recently, much attention has been paid to land mine problem as it represents a serious threat to civilian population in several parts of the world. However, there exists another related and perhaps more widespread environmental problem which is the presence of the Unexploded Ordnance (UXO) in many countries and in particular in USA. There are currently over 9,000 Formerly Used Defense Sites (FUDS) in continental USA, some of them of vast acreage, which are now in public or private ownership. Of the 9,000 FUDS, over 2,000 have been identified as having the potential for contamination by UXO and thus require site remediation.

A key and challenging task in site remediation is the detection of the subsurface UXOs. This task is currently performed by humans walking through the site and using detection devices such as magnetometer and gradiometer. This is not only a dangerous activity, but is also extremely time consuming, costly, and inefficient. In fact, it can cost anywhere between \$1,000 and \$20,000 per acre depending on the anomaly and ordnance concentration, depth, and field conditions such as heavy brush and steep terrain [1]. Given the time and cost involved in remediation of a large number of sites, some of them of vast acreage, novel technologies are needed to enable a rapid and cost-effective site survey and detection of subsurface UXO.

Airborne, ground penetrating, SAR has the potential of an ideal technology for a rapid and cost-effective site survey. However, though it is being increasingly used as an effective remote sensing technology, it has not previously been validated as a viable tool for subsurface UXO detection. In fact, previous experiments at Jefferson Proving Ground seemed to indicate that this technology is not suitable for subsurface UXO detection [1]. There are two main challenges in using airborne, ground penetrating, SAR data for UXO detection [2] (see also Sec. 2):

1. Highly negative signal-to-clutter environment, and
2. Low-resolution measurement, due to the small size of the class of UXOs of interest with respect to the SAR wavelength resulting in a subpixel target.

In 1995, US Army Corps of Engineers, Engineering and Support Center, Huntsville (CEHNC), JPL, and SRI conducted the largest ever airborne, ground penetrating SAR survey for UXO detection and site characterization at a

highly contaminated FUDS, the former Camp Croft Training Facility in Spartanburg, SC [2,3]. This was a first operational validation of a remote sensing technology that had never been applied for a large scale (> 19,000 acres) UXO site remediation activity in the past. Not only was the Camp Croft site of vast acreage but also the extent of OE contamination was undocumented and unknown. In addition, it presented significant complexity in foliage clutter and terrain relief.

The JPL team, for the first time, developed effective and advanced post-processing algorithms for detection of subpixel target in a highly negative signal-to-clutter environment, using SAR data from Camp Croft [2]. These algorithms were first successfully validated against ground truth data (found UXOs by walk-through of the site) provided by the CEHNC. Upon this successful validation, they were then applied to a survey of a small area (100 acres) of Camp Croft. Subsequent inspection of this area by CEHNC clearly validated the effectiveness of JPL algorithms for both detection of subsurface UXOs and identification of clear areas [4]. JPL's successful results of this challenging and real-life case study for the first time clearly established the airborne, ground penetrating, SAR as a viable remote sensing tool for a rapid and cost-effective survey of large sites.

As a result of successful validation and application on a small-scale, the CEHNC has considered several sites (representing some of the current site remediation projects at CEHNC) for a large-scale application, demonstration, and validation of JPL's technology. Former Buckley Field, Colorado, is the first selected application site. This is a 60,000 acre FUDS located on the semi-arid high plains outside Denver. Ordnance remediation at this site is of major and critical importance because of increasing urban development in the area. In preparation for such a large-scale survey, JPL has been developing advanced algorithms and a high-performance testbed for processing of massive amount of expected SAR data from this site. Two key requirements of this project are the accuracy (in terms of UXO detection) and speed of SAR data processing. The first key feature of this testbed is a large degree of automation and a minimum degree of the need for human perception in the processing to achieve an acceptable processing rate of several hundred acres per day. For accurate UXO detection, novel algorithms have been developed and implemented. These algorithms analyze dual polarized (HH and VV) SAR data. They are based on the correlation of HH and VV SAR data and involve a rather large set of parameters for accurate detection of UXO. For each specific site, this set of parameters can be optimized by using ground truth data (i.e., known surface and subsurface UXOs). In this paper, we discuss these algorithms and their successful application for detection of surface and subsurface anti-tank mines by using a data set from Yuma proving Ground, AZ, acquired by SRI SAR.

2. YUMA SAR DATA SET

In July and October 1995, the MIT Lincoln Laboratory and Army Research Laboratory (ARL) conducted a ground penetrating radar experiment at the U.S. Yuma Proving Ground in Arizona [5]. Three radar systems, the SRI Folpen III, the ARL BoomSAR, and the Navy P-3 collected polarimetric data from both targets and clutter. Some of the targets deployments included a mine field, wire/pipes, and missile clones. In this paper, we only consider the data collected by SRI airborne Folpen III SAR over the deployed minefield.

Figure 1 shows an aerial photograph of the Philips Drop Zone at Yuma Proving Ground wherein the rectangle indicates the location of the deployed minefield. Figure 2 shows the pattern of deployed mines and their burial depth. Note that at the first, second, third, and sixth row the M20 anti-tank mines (shown in Figs. 3-4) are deployed. The row 4 contains an unknown type of plastic mine which cannot be detected by SAR. Also, the row 5 includes smaller M12 anti-tank mines which, due to their small size, are not detectable. In the following, we only concentrate on the detection of M20 anti-tank mines. Note that, given their size (Fig. 3) and SRI SAR 80cmx80cm resolution, the M20 anti-tank mines represent subpixel targets.

Figures 5 and 6 show the VV and HH magnitude polarization of radar image. The bright spots at the upper left and lower right corners of these images indicate the ground reflectors deployed in this experiment to better identify and register the location of the minefield. Also, interestingly, the two bright and long lines going across the minefield in both images are due to the presence of two 100-meter electrical wires with a diameter of 2.7 mm; one laid on the ground surface and the other buried at 30cm below the surface. As can be seen, only a very few of the M20 anti-tank mines can be clearly distinguished in these images. In fact, these images represent the typical case of negative signal-to-clutter environment usually encountered in SAR data analysis.

Figures 7 and 8 show the VV and HH phase polarization of radar image. The only noticeable information in these two images are the phase shift resulting from long objects, i.e., the electrical wires.

3. JPL AUTOMATIC TARGET DETECTION ALGORITHM

The techniques reported in this paper are based on finding local maxima in SAR images. The assumption is that a detectable target anomaly will be associated with one or more of these local maxima. In general, an image will have a great many local maxima which do not correspond to target anomalies. Not surprisingly, some of these local maxima seem to be much better candidates than others. The challenge is to find effective algorithms that down select a local maximum which is a poor candidate and thereby eliminate false positives. Our experience seems to indicate that there is no single effective algorithm for this. However, it does appear that a series of down selection algorithms,

each by itself marginally effective, can together be moderately effective in selecting good candidates from among all the local maxima.

3.1. Finding All Local Maxima in an Image

For convenience, an image is always treated to be a real-valued function f on the $Z \times Z$ plane of integers. A local maxima is any maximal connected subregion R of $Z \times Z$ for which f assumes a constant value M and $f(p) < M$ for any pixel p adjacent to R . For instance, the image f may assume the constant value 200 on a 3×3 square of pixels and assume values less than 200 at any of the 16 adjacent pixels surrounding this square. This 3×3 square is then a local maxima. In finding local maxima, Z is set to 3, that is, every pixel is compared with its immediate neighbor in a recursive fashion. Most local maxima consist of a single pixel. However, adjacent pixels having the same intensity will result in local maximum that is more than one pixel.

3.2. Removal of Large Objects

This kernel of the algorithm classifies local maxima in terms of their size and shape by determining the properties of the objects. This is done in terms of diameter from one end to the other end of any object based on the connectivity of the higher intensity values. The assumption is that if a local maximum corresponds to a peak having a diameter of a given size or larger, then it probably identifies to some feature which is too large to be considered as a target anomaly. The subregions that make up large objects are tagged and the corresponding pixels are not taken into account in the later calculations.

The large object removal kernel employs four parameters two for each polarization: a threshold value for HH polarization (T_{HLOR}), a threshold value for VV polarization (T_{VLOR}), a diameter value for HH polarization (D_H), and a diameter value for VV polarization (D_V). The diameter values are used to classify the size of objects. It should be emphasized that this kernel is compute intensive as it requires the analysis of every pixel in connection with its neighboring pixels. Therefore, the threshold values are used to reduce the scope of computation. Note, also, that the signature of large objects and in particular surface objects are usually brighter, i.e., they have a higher pixel value. Examples of this phenomena are the bright signature of electrical wires and ground reflectors in Figs. 5 and 6. Note that these four independent parameters need to be optimized for each data set since a number of site dependent factors (e.g., vegetation, roads, slopes, pipes, power cables, fences, etc.) can influence their optimal values.

3.3. Local Normalization

This kernel performs a local analysis of the retained local maximum. It applies the following procedures for every retained local maximum in both HH and VV polarized images by setting a square window size of $(2n+1)$ by $(2n+1)$ centered at the local maxima.

- Compute the local average of the window:

$$\text{avg} = \frac{\text{the sum of all pixels in the window}}{(2n+1)^2}$$

- Compute the local standard deviation of the window:
 $\text{sigma} = \frac{\text{the sum of SQRT of every pixel} - \text{avg}}{(2n+1)^2}$
- Compute the deviation from the local average of the local maxima:
 $\text{deviation} = (\text{locmax} - \text{avg}) / \text{sigma}$

The calculated deviation for each pixel in the window becomes its new magnitude and is used in the subsequent calculations. Note that the window size, which is determined by n , is one of the parameters that needs to be optimized for every data set.

3.4. Thresholding

Once the new magnitudes are assigned to the pixels as described above, this kernel is used to eliminate a major portions of false positives by excluding all local maxima whose new magnitude (i.e., deviation) is below a certain level. This thresholding process is performed on both normalized HH and VV polarized images. However, as stated before, targets and clutter can manifest themselves quite differently in each polarization. Therefore, two independent parameters, T_H for HH polarization and T_V for VV polarization, are used as threshold values. Note that the two independent parameters, T_H and T_V , need to be optimized for every data set.

3.5. Correlating Multiple Images

This kernel takes two different SAR images (HH and VV polarized magnitude) of exactly the same region and finds those retained local maxima that are common to both images. This process is referred as *correlating* the local maxima.

The assumption is that if there are two retained local maxima, one in each image, which are approximately in the same location, then this location is much more likely to correspond to a target anomaly and not to a false positive.

Note that an exact match between two images of the same area is unlikely due to a number of inherent factors including the way HH and VV polarized data are acquired. That is, the signature of an object might appear in two images with some pixel shift. Because an exact match is unlikely, a parameter is introduced to take into account the pixel shift. Using this parameter, called *pixel shift* (PS), the two images are then expanded and superimposed so that nearby local maxima overlap. Final thresholding (C_{th}) is then applied on the combined image. The resulting image is a set of local maxima that represent likely targets. Again, the parameters, PS and C_{th} , need to be optimized for each data set.

3.6. Parameters Optimization

The algorithm described above utilizes eight independent parameters (T_{HLOR} , T_{VLOR} , D_H , D_V , T_H , T_V , PS, and C_{th}) to achieve the best possible result in target detection. Using a set of ground truth data (i.e., known UXOs) for any given site, these parameters can then be optimized to extract information as much as possible for analysis of the whole site. The optimization process is performed by running all

possible values of the parameters and scoring the results against the ground truth data.

For Yuma data set, a target file consisting of all the mines on the first, second, third, and sixth rows has been generated. Appropriate range of values has then been identified for each parameter. The algorithm was then run with all possible cases covering the range of values of parameters. This optimization process, due to its inherent combinatorial nature, is extremely compute-intensive. In fact, for Yuma data set, it involved on the order of 50,000 cases to determine the best combination of parameters. On a typical workstation, this optimization might have taken weeks to be completed. In order to achieve a fast turnaround time a highly parallel architecture, Linux-based BEOULF with 32 processor nodes, was used. By exploiting the computing power of this architecture and the data parallel nature of the optimization (i.e., each processor can independently run a subset of cases), a very fast turnaround time of less than a day was achieved.

4. RESULTS OF MINE DETECTION USING YUMA SAR DATA SET

In this section, we discuss the results of optimized algorithm for detection of anti-tank mines by using the Yuma Proving Ground SAR data set. Figure 9 shows the resulting image from the application of our algorithm to the minefield without applying Large Objects Removal kernel. Although, a significant reduction in clutter has been achieved, the large objects (i.e., electrical wires and ground reflectors) are still present in the image. Figure 10 shows the results with Large Objects Removal. As can be seen in Fig. 10, the large objects have been successfully eliminated from the image.

Figure 11 shows the pattern of anti-tank mines laid on the first row. Figure 12 shows the pattern of resulting anomalies (both targets and false positives). Figure 13 shows the impact of only one parameter, the final parameter C_{th} , while keeping all other parameters fixed at their optimum values, on the detection rate of the algorithm for first row. The key point is that, using our parameterization, it is possible to optimize the algorithm so that maximum target detection with minimum false positives and misses can be achieved. Note that, as our experiments with this data set have shown, such target detection rate cannot be achieved by just applying a simple thresholding as proposed in [5].

Figure 14 shows the pattern of anti-tank mines laid on the third row. Figure 15 shows the pattern of resulting anomalies (both targets and false positives). Figure 16 shows the impact of only one parameter, the final parameter C_{th} , while keeping all other parameters fixed at their optimum values, on the detection rate of the algorithm for the third row. As can be seen and compared with the first row, a much better result in terms of target detection with minimum false positives and misses has been achieved. This better result can be attributed to the fact that the signature of the

electrical wires does not strongly interfere with the third row. Similarly, the signature of the electrical wires does not interfere with the sixth row leading to comparable results as those of the third row. Figures 17-19 show the results for the sixth row.

5. CONCLUSION

In this paper we presented a novel algorithm for detection of subpixel targets in highly negative signal-to-clutter ratio environment by using airborne, ground penetrating SAR data. The fact that airborne, ground penetrating, SAR has not previously been successful in subsurface UXO detection can be mainly attributed to the lack of adequate processing technique. Traditionally, simple thresholding is applied to either HH or VV polarized data. The first drawback of this approach is that, in a negative signal-to-clutter ratio environment, only the strongest targets with a large number of false positives can be detected. The second drawback is that of using only one image is that it does not allow the extraction of maximum information possible by multiple images. In contrast, our parameterized technique including correlation, allows exploitation of dual polarized data with a much better optimization for target detection with minimum false positives and misses.

We are currently improving and enhancing the technique discussed in this paper. In particular, there has not yet been any proposed technique for exploitation of information provided by the SAR phase images. We strongly believe that phase images can be effective in improving our results. However, the challenge is in the development of adequate techniques for extraction of information from phase images. We are currently investigating new techniques for processing of phase images by using wavelet transforms.

6. ACKNOWLEDGEMENT

The research described in this paper was performed at the Jet Propulsion Laboratory, California Institute of Technology, under the contract with National Aeronautics and Space Administration (NASA). This work was supported by the U.S. Army Corps of Engineers, Omaha District and Engineering and Support Center, Huntsville. We would like to acknowledge the kind support of Stanford Research Institute (SRI) and particularly Drs. Roger Vickers and Werner Graf for their assistance and for providing us with the Yuma SAR data set.

7. REFERENCES

- [1] J. Potter, US Army Corps of Engineers, Engineering and Support Center, Huntsville, *Personal Communication*, 1996.
- [2] A. Fijany, R. Mackey, S. Gulati, V. Daggumati, "Innovative Ground Penetrating SAR processing Algorithms for UXO Detection at Camp Croft, SC."

Proc. UXO Forum 97, pp. 88-101, May 1997.

[3] J. Meloy and R. Vickers. "Ultrawideband Synthetic Aperture Radar Mapping of Camp Croft." SRI Final Report 6561, July 1996.

[4] Double-Blind Detection Survey by Ground Penetrating SAR of UXO Contamination at Camp Croft, SC.. Final Report, OE-CX, Army Engineering and Support Center, Huntsville, July 1997.

[5] C.F. Lee et al , " Results and analysis of the 1995 Yuma ground penetrating radar experiment.," Proc. UXO Forum 96, pp. 405-414, May 1996.

8. BIOGRAPHY

Dr. Amir Fijany is a Senior Member of Technical Staff with the Ultra Computing Group, Information and Computing Technologies Research Section, at the Jet Propulsion Laboratory, and a Visiting Associate at the California Institute of Technology. He received the BS and MS degrees in electrical engineering from University of Tehran in 1980, and the D.E.A. and Ph.D. degrees in electrical and computer engineering from University of Paris XI (Orsay), France, in 1981 and 1988, respectively. In 1987, he joined JPL and since May 1996 he is also a Visiting Associate at the California Institute of Technology. His research activities include signal processing with application to ground penetrating SAR, parallel algorithms, advanced computer architectures, and application of parallel computing to scientific and Grand Challenge problems. He holds five U.S. patents on the design of parallel architectures for signal processing and robotics applications. He has received over 20 NASA Technical Innovation Awards. He has authored over 60 articles in archival journals and conference proceedings as well as three book chapters. Dr. Fijany is a Senior Member of IEEE.



Figure 1: Aerial photo of Philips Drop Zone at Yuma Proving Ground, Arizona. The rectangle in the upper right corner denote the minefield.

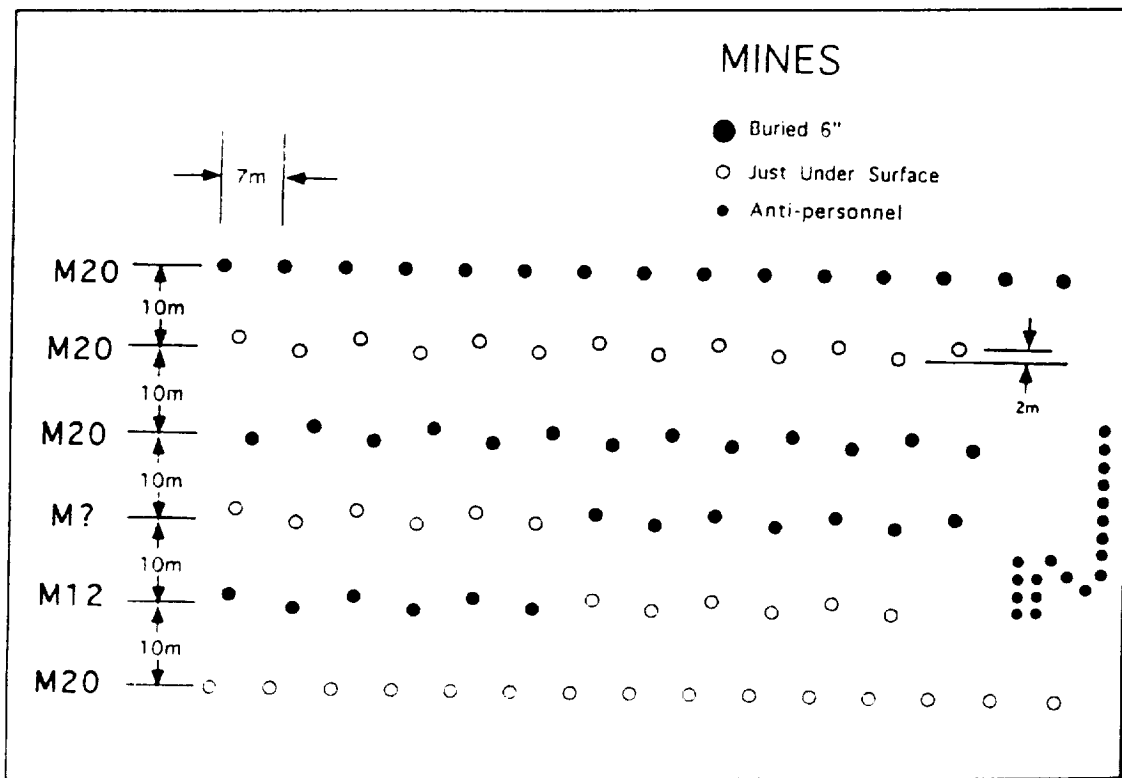


Figure 2: Location and pattern of mines and mine types buried in the minefield.

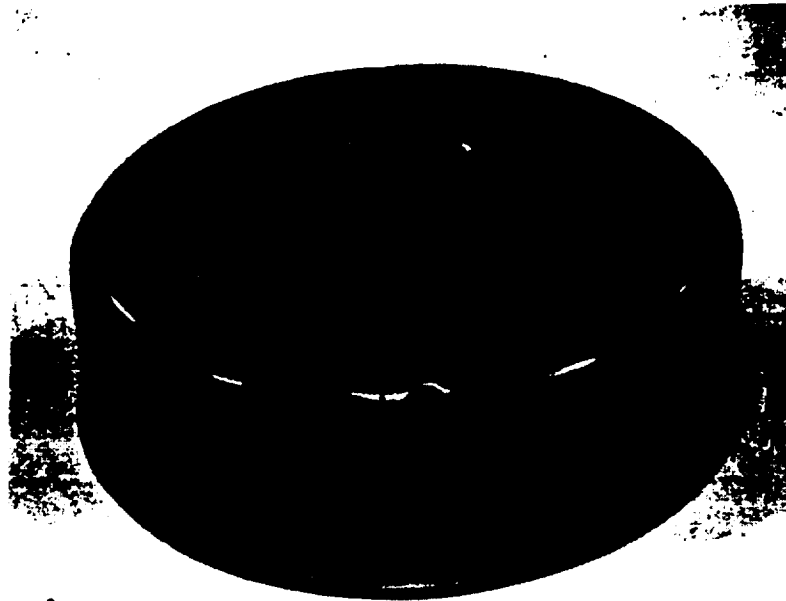


Figure 3: M20 Anti-tank mine

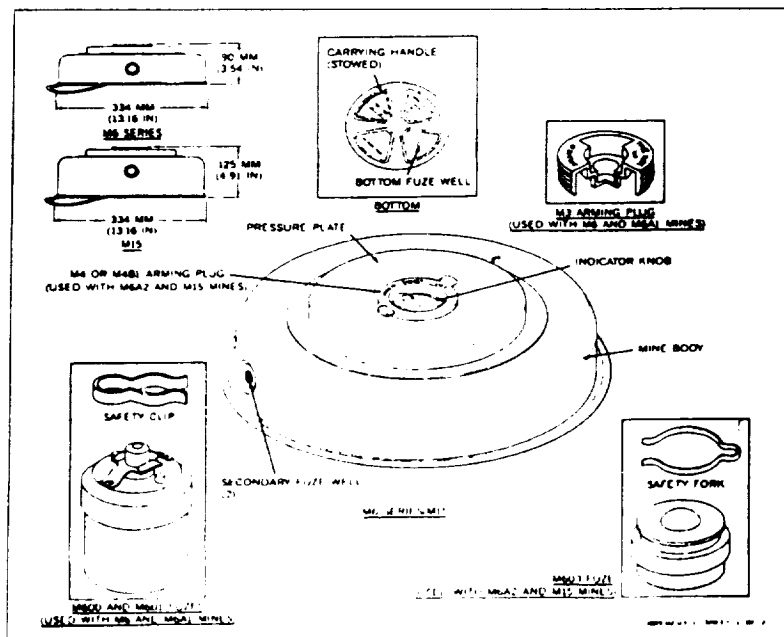


Figure 4: M20 Anti-tank mine schematics

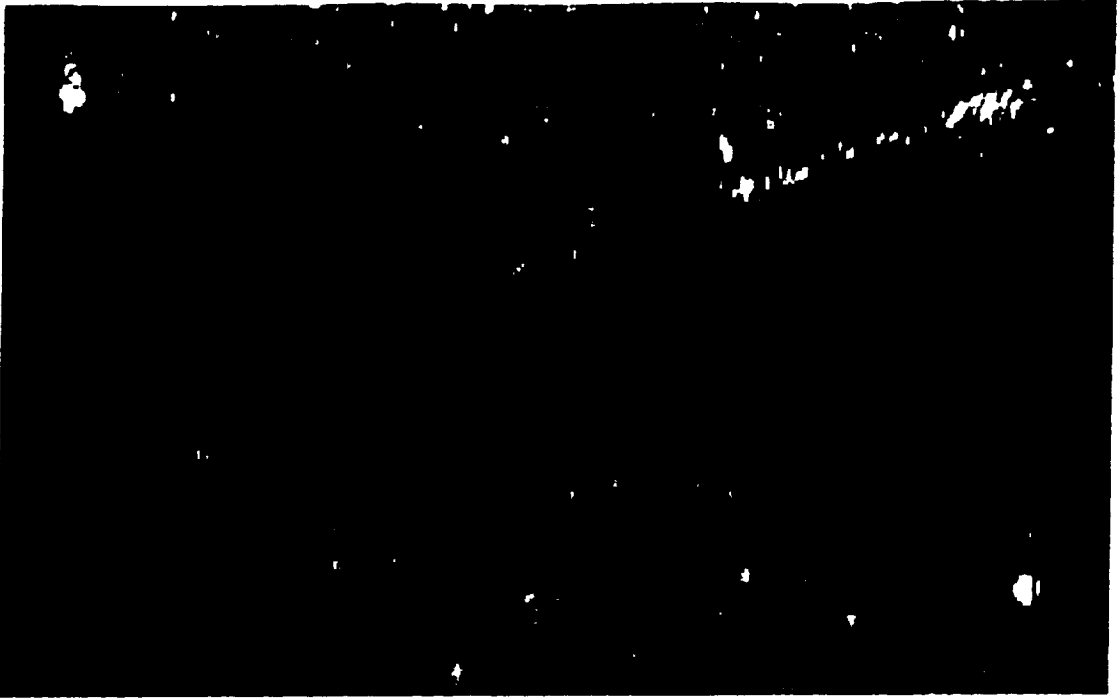


Figure 5: A Magnitude 17 star field in the solar image of the mission field

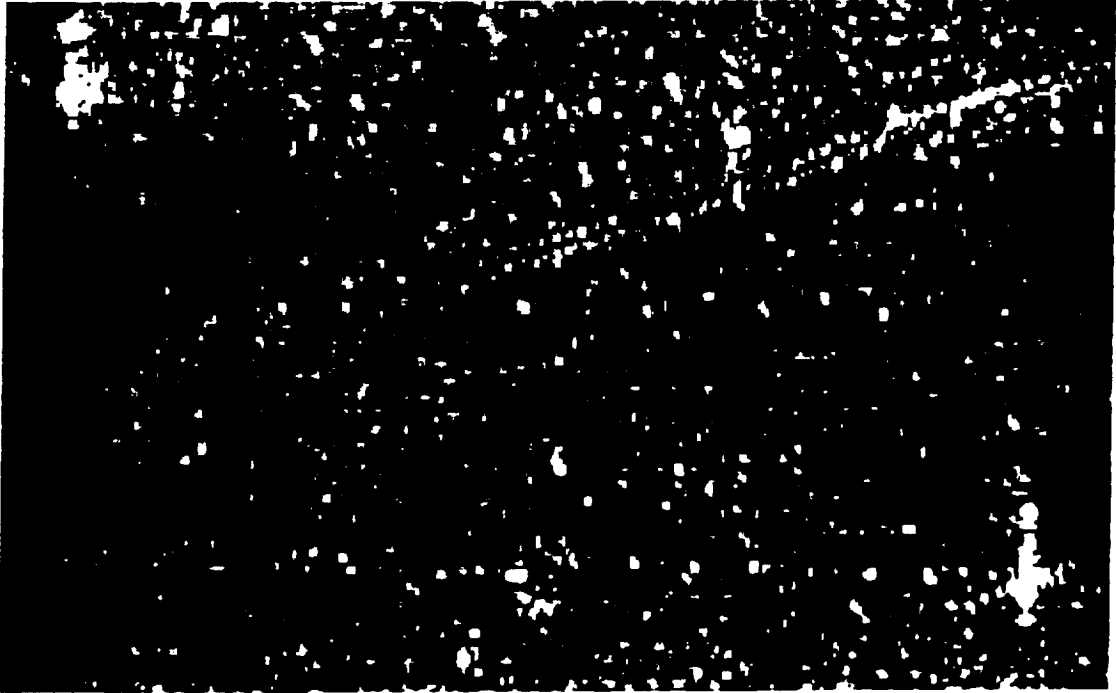


Figure 6

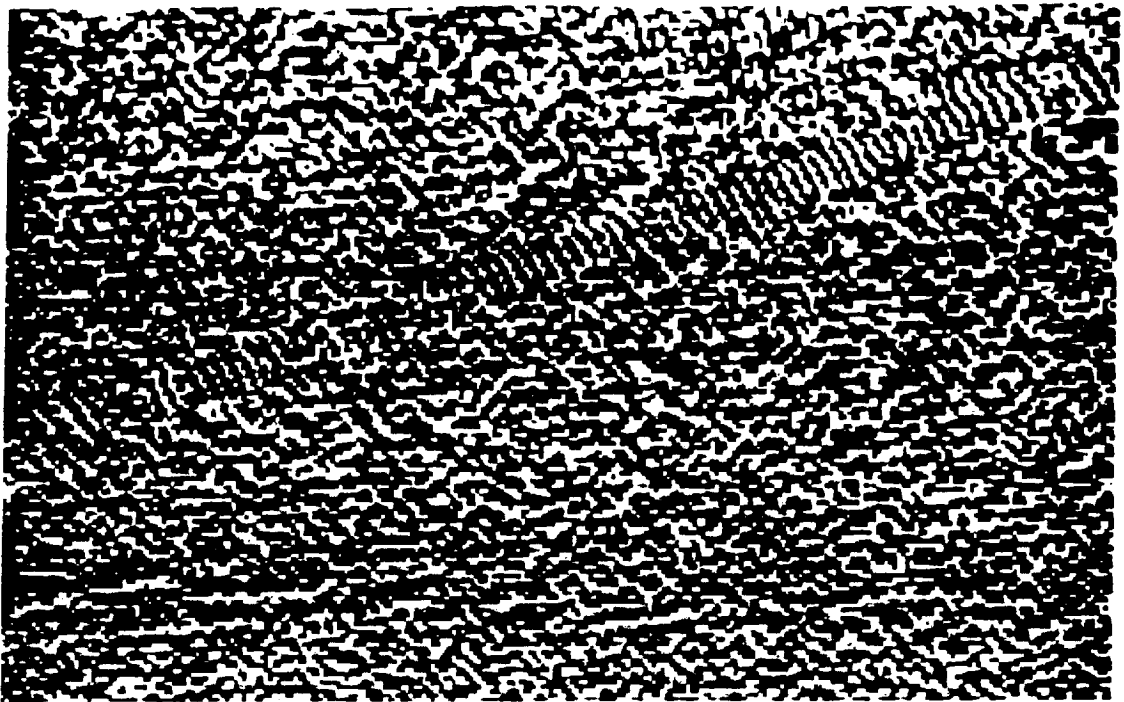


Figure 7: VV Phase Polarization of the radar image of the minefield.

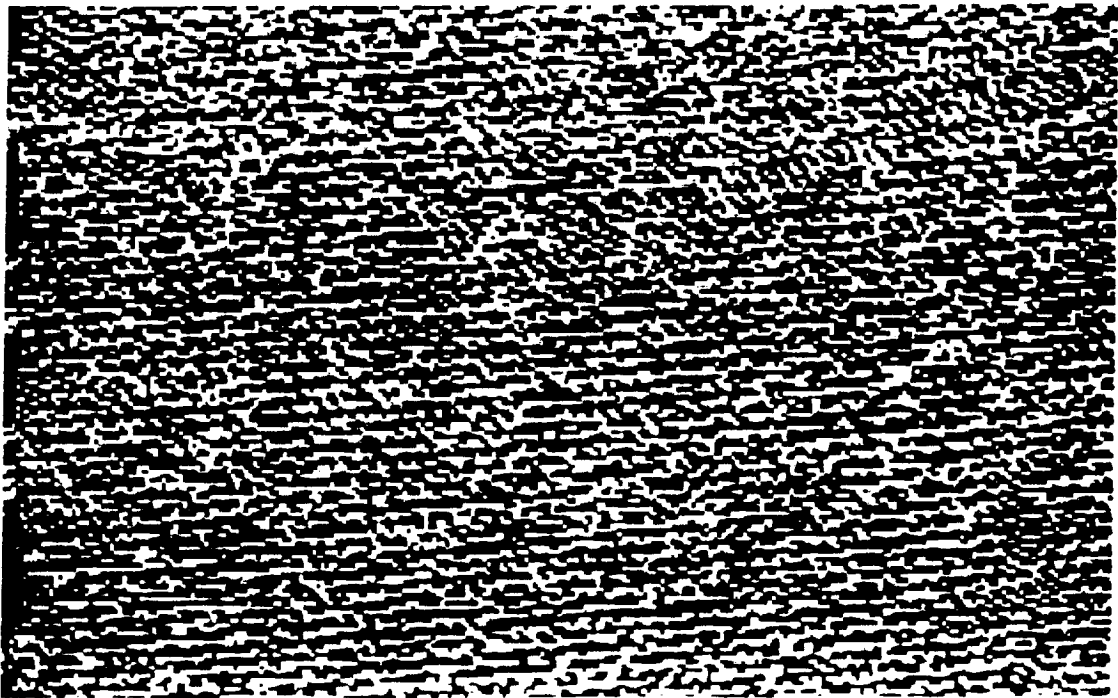


Figure 8: HH Phase Polarization of the radar image of the minefield.

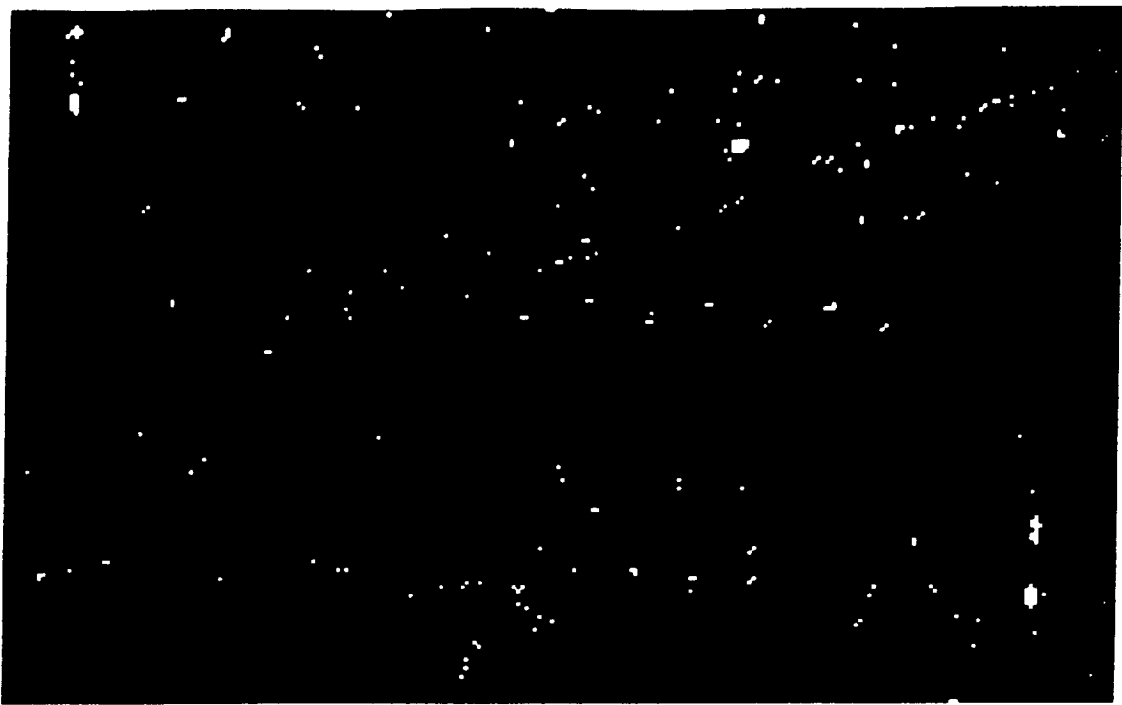


Figure 9: \log_{10} of the number of objects per pixel as a function of the processing time. The x-axis is labeled "Processing time (min)" and ranges from 0 to 20. The y-axis is labeled " \log_{10} of the number of objects per pixel" and ranges from 0 to 2. The data points show a general upward trend, indicating that the number of objects per pixel increases as the processing time increases.

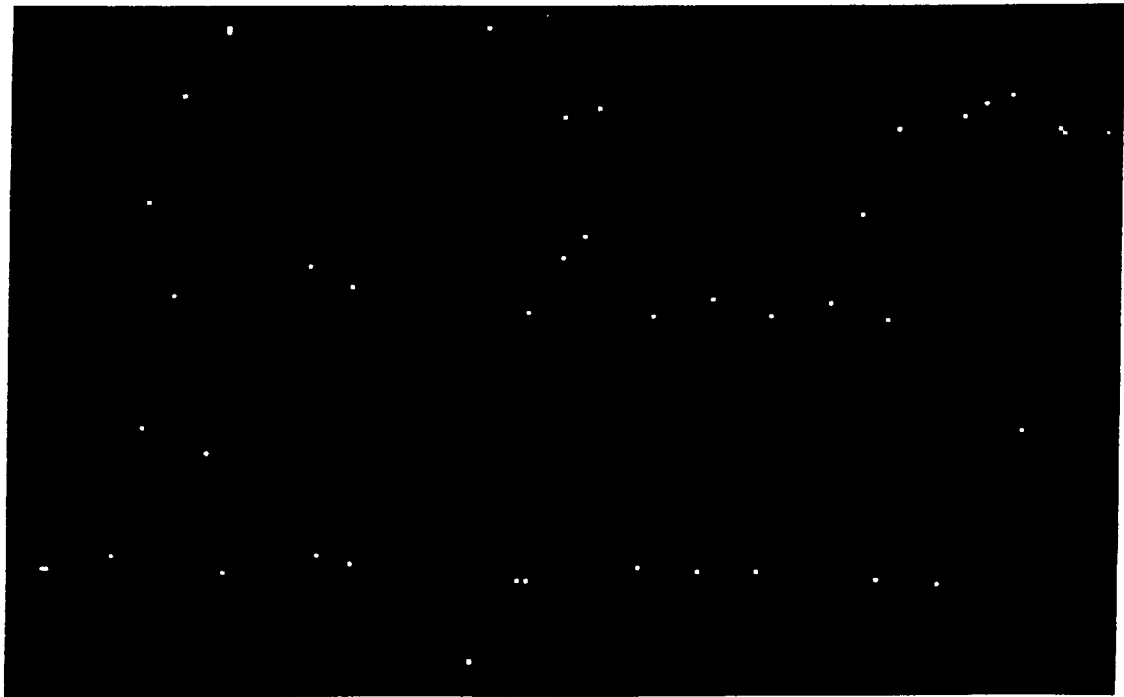


Figure 10: \log_{10} of the number of objects per pixel as a function of the processing time. The x-axis is labeled "Processing time (min)" and ranges from 0 to 20. The y-axis is labeled " \log_{10} of the number of objects per pixel" and ranges from 0 to 2. The data points show a general upward trend, indicating that the number of objects per pixel increases as the processing time increases.

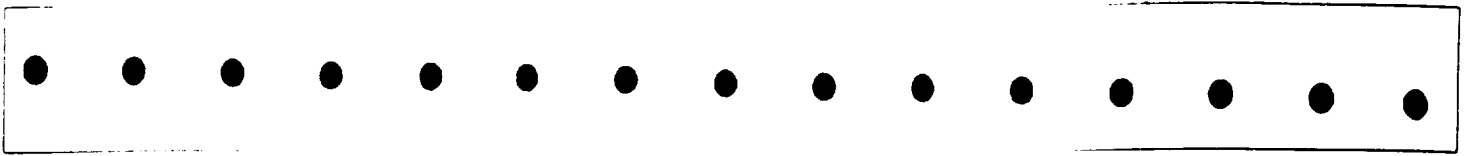


Figure 11: The pattern of mines laid out on the first row in the minefield.

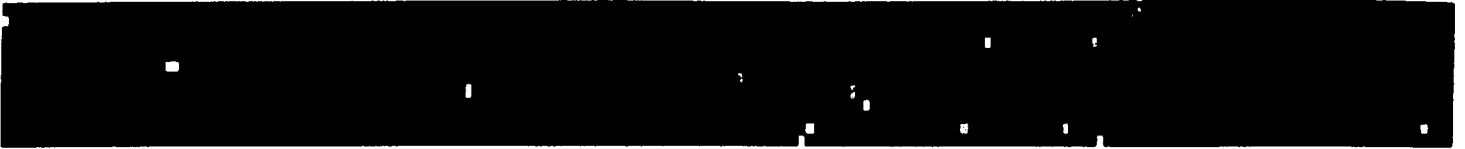


Figure 12: Signature of M20 mines at a depth of 6 inches below surface resulting from the application of post processing algorithm on the first row.

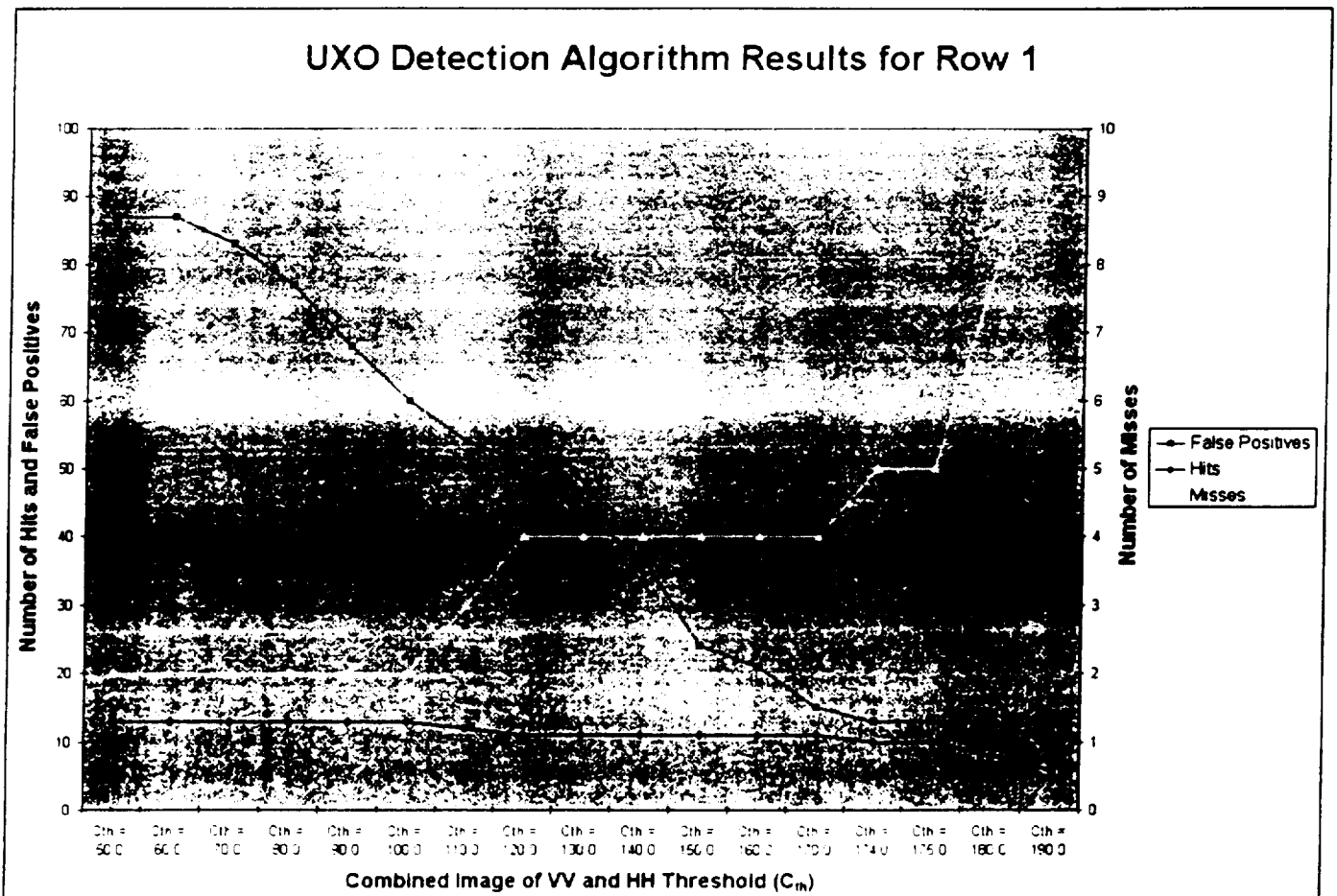


Figure 13: Detection Rate vs. Combined Image Threshold. Notice how number of False Positives and Hits decrease and Misses increase as threshold values increase. The optimal value is when Hits is at maximum and False Positives and Misses are at minimum which intersect at around combined threshold value of 175.0

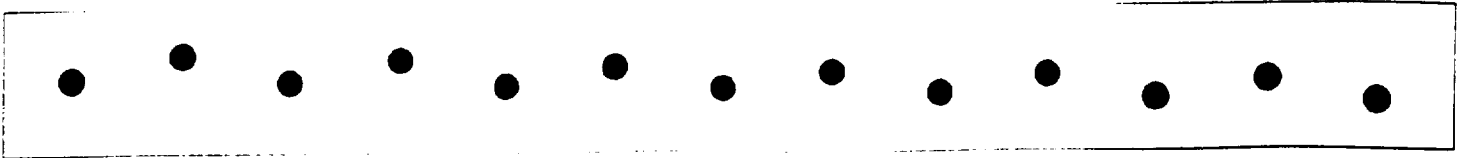


Figure 14: The pattern of mines laid out on the third row in the minefield.

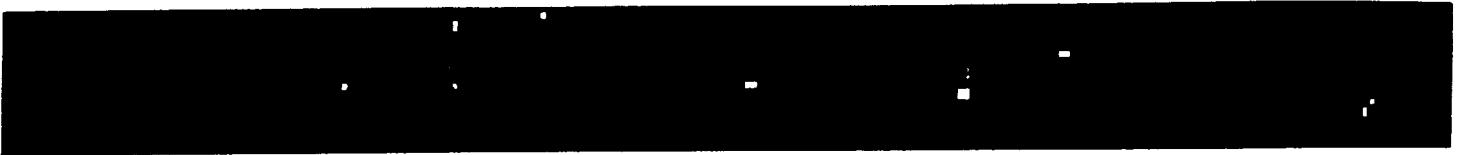


Figure 15: Signature of M20 mines at a depth of 6 inches below surface resulting from the application of post processing algorithm on the third row.

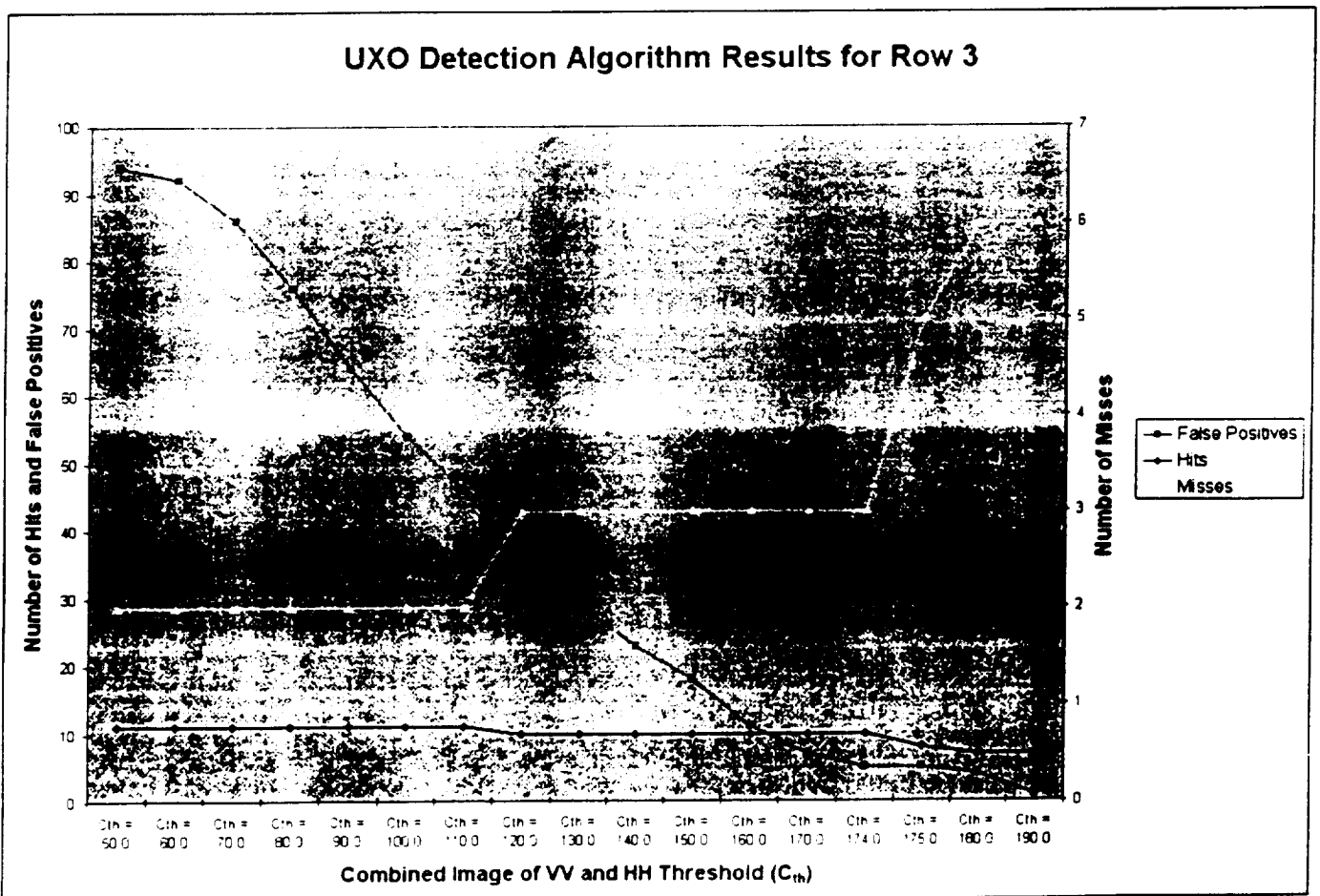


Figure 16: Detection Rate vs. Combined Image Threshold. Notice how number of **False Positives** and **Hits** decrease and **Misses** increase as threshold values increase. The **optimal value** is when **Hits** is at maximum and **False Positives** and **Misses** are at minimum which intersect at around combined threshold value of 174.0

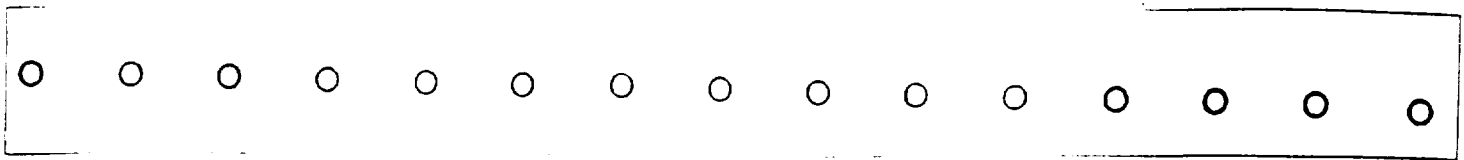


Figure 17: The pattern of mines laid out on the sixth row in the minefield.

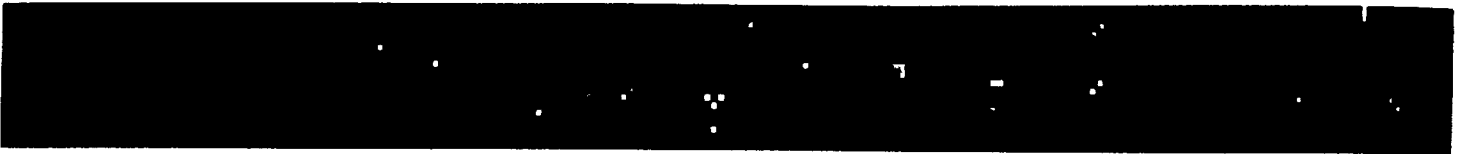


Figure 18: Signature of M20 mines just below surface resulting from the application of post processing algorithm on the sixth row.

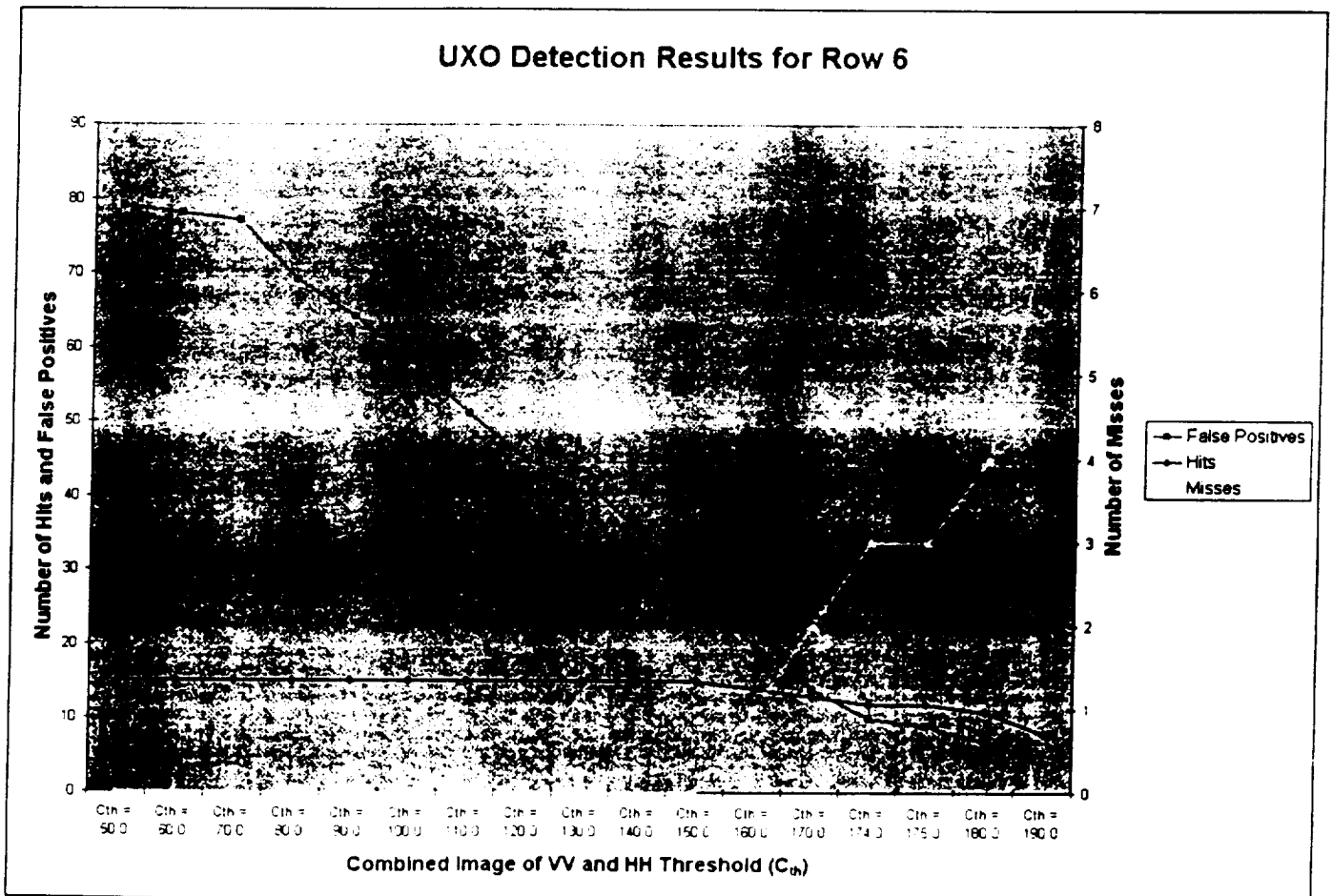


Figure 19: Detection Rate vs. Combined Image Threshold. Notice how number of **False Positives** and **Hits** decrease and **Misses** increase as threshold values increase. The **optimal value** is when **Hits** is at maximum and **False Positives** and **Misses** are at minimum which intersect at around combined threshold value of 175.0